



Catalytic decomposition and reduction of N₂O over micro-mesoporous materials containing Beta zeolite nanoparticles

M. Rutkowska^{a,*}, L. Chmielarz^a, D. Macina^a, Z. Piwowarska^a, B. Dudek^a, A. Adamski^a, S. Witkowski^a, Z. Sojka^a, L. Obalová^b, C.J. Van Oers^c, P. Cool^c

^a Jagiellonian University, Ingardena 3, 30-060 Kraków, Poland

^b Technical University of Ostrava, 17. listopadu 15, 708 33 Ostrava, Czech Republic

^c University of Antwerpen, Universiteitsplein 1, B-2610 Wilrijk, Belgium

ARTICLE INFO

Article history:

Received 30 October 2012

Received in revised form 28 March 2013

Accepted 6 May 2013

Available online 14 May 2013

Keywords:

Nitrous oxide

Catalytic decomposition

Beta zeolite

Zeolite nanoparticles

ABSTRACT

Zeolitic materials with combined micro and mesoporous structure were synthesized using two different approaches. A first series of the samples was obtained by impregnation method. Suspension of Beta nanoparticles was impregnated on SBA-15 mesoporous silica. In the second synthesis route, called non-templating method, Beta nanoparticles were aggregated under specified conditions with the formation of micro-mesoporous material (without the use of the mesopore directing agent). Micropores were present in the zeolite nanoparticles, while mesopores were located in the interparticle space. The combined micro and mesoporous structure of the obtained materials, exhibiting the properties of Beta zeolite, was confirmed by nitrogen sorption measurements, XRD, TGA and DRIFT techniques. The hierarchical porous structure of the samples resulted in an improved accessibility of ion-exchange positions in comparison to conventional Beta zeolite and allowed the introduction of iron, nearly exclusively in the form of monomeric Fe³⁺ cations and oligomeric Fe_xO_y species. The iron modified micro-mesoporous samples as well as SBA-15 and Beta zeolite (as reference samples), were tested as catalysts of N₂O decomposition. The most promising micro-mesoporous sample (Fe-Beta/meso) was tested as catalyst in the reactions of N₂O decomposition and N₂O reduction with CO at different composition of gas mixture (in the presence of O₂, H₂O and NO). Catalytic activity of iron-exchanged, micro-mesoporous Beta and conventional Beta zeolites in the reaction of N₂O conversion was very similar.

© 2013 Elsevier B.V. All rights reserved.

1. Introduction

Nitrous oxide, due to its very high global warming potential (GWP_{N₂O} ≈ 310 GWP_{CO₂}), and atmospheric lifetime (about 120 years), is considered as one of the most dangerous greenhouse gasses. Moreover, N₂O is converted into NO and NO₂ in stratosphere, thereby contributing to the destruction of ozone layer. For these and also economic (taxes for emissions) reasons, development of the effective N₂O abatement methods is in a spotlight of scientists interest. Emission of N₂O from nitric acid plants, beside its emission from adipic acid installations, is the largest among the industrial sources. Several options of N₂O emission abatement are available, but its catalytic decomposition to N₂ and O₂ seems to be the most promising method [1–3]. Two possible locations of the catalytic N₂O converts were proposed in the installation for nitric

acid production [2]. The first one is just behind the Pt-Rh catalyst for NH₃ oxidation, inside the ammonia burner, where temperature is about 1173 K (high-temperature N₂O decomposition). The second option is the placement of the N₂O converter in the end of pipe (downstream of the absorption column), where temperature of exhaust gases is about 523–773 K (low-temperature N₂O decomposition). Because the first option requires an intervention to the ammonia burner construction and additionally, extreme thermal stability of the catalyst, therefore the low temperature process seems to be an interesting alternative of the limitation of N₂O emission in such installations. For these reasons, the recent studies are focused on development of the catalysts, which will be able to effectively operate at temperatures below 773 K in the presence of all components of exhaust gases, such as oxygen, water vapor and NO (the product of ammonia oxidation in nitric acid plants).

Zeolites are well known as active catalysts for oil refining, petrochemistry, organic synthesis (in case of molecules with diameter < 10 Å) [4] and many different environmental processes, including N₂O decomposition (especially iron modified zeolites

* Corresponding author. Tel.: +48 126632096; fax: +48 126340515.

E-mail address: rutkowsm@chemia.uj.edu.pl (M. Rutkowska).

such as Fe-MFI, Fe-USY, Fe-silicate, Fe-BEA [5–11]. Despite many advantages of zeolites, such as pure crystalline structure, high surface area, variety of structures–size and shape selectivity, absorption and ion-exchange properties as well as controlled concentration and strength of acid sites, in some processes their major drawback is the presence of narrow pores of typical diameter below 1.2 nm, which limits diffusion rate of reactants. Moreover, the active centers located within micropores are not available for bulky compounds, thus application of zeolites is limited to the conversion of relatively small molecules [12–15]. This problem could be solved by development of the zeolitic systems with hierarchical – micro and mesoporous structure. Several strategies to obtain such hierarchical micro-mesoporous composites with improved accessibility of acid sites have been proposed. The main strategies can be divided into three paths: (i) an increase of zeolite pore diameters, (ii) a decrease in zeolite crystals size and (iii) generation of large pores inside zeolite crystals.

The most common way of the mesopore formation in zeolites is their desilication (base leaching). Groen et al. [16–20] extracted framework silicon using a solution of NaOH (0.2 M) to make this process slower and therefore more controllable. Abelló et al. [21] used 1 M aqueous solutions of organic bases such as TPAOH and TBAOH. On the other hand Sadowska et al. [22] used a mixture of NaOH and TBAOH for the extraction of framework silicon from the zeolite structure. The procedure of silicon extraction can be optimized and controlled using different types and concentrations of bases as well as duration of the leaching process [23,24].

Templating is another, widely used method for the generation of mesopores in the zeolite materials. Egeblad et al. [25] categorized templating methods into three types: (i) solid templating, (ii) supramolecular templating and (iii) indirect templating. The use of different templates with specific macromorphological features allows controlling the shape and size of channels in the zeolite structure. Latex beads, polymers (e.g. polystyrene beads), silica-containing biotemplates (e.g. leaves, stems), carbon blacks (pearls, fibers, spheres, nanofibers and nanotubes) were proposed as templates [26,27]. Typically, such templates are impregnated with zeolite precursor solution, followed by hydrothermal treatment, which accelerates the zeolite crystals growth around templates. The supramolecular templating (double templating) method is based on the formation of the organized micellar structures, which play a role of templates for the formation of intercrystalline or intracrystalline mesopores in zeolite. Both molecular (micropores) and supramolecular (mesopores) templates are used in the one-step synthesis.

Apart from the mentioned above major methods there are many other synthesis routes, such as recrystallization of the amorphous mesoporous materials in the presence of micropore directing agent [28], pillaring or delamination of layered zeolites [29], generation of zeolite nanoseeds and their further aggregation around solids or supramolecular templates [30–32].

Our research was focused on the synthesis of hybrid micro-mesoporous materials with the zeolitic properties using two modern approaches. The first method was based on deposition of Beta zeolite nanoparticles on SBA-15 by wet impregnation. This method was described by Meynen et al. [33], who deposited silicate-1 nanoparticles on the surface of mesoporous silica. It was shown that the obtained materials with the combined micro-mesoporous structure were characterized by the improved diffusion efficiency of the selected molecules comparing to silicate-1 [33]. The second method is based on the controlled aggregation of Beta zeolite nanoparticles and results in the formation of the mesoporous interparticle structure. This method, described by Van Oers et al. [34], does not need any templates for the generation of mesopores.

The obtained samples, modified with iron, were examined in the role of catalysis for N_2O decomposition and reduction.

2. Experimental methods

2.1. Catalysts preparation

The first step of the synthesis was preparation of nanoparticles suspension by mixing 21 mL of tetraethylammonium hydroxide (TEAOH, 35%, Sigma–Aldrich) with 8.4 mL of double distilled H_2O , 4.5 mL of 3.7 M HCl (37%, Sigma–Aldrich) and 5 g of fumed silica (Aerosil 200, Evonic) followed by stirring of the resulting mixture for 30 min. Parallely, in the second batch, 0.3812 g of NaAlO_2 (Sigma–Aldrich) was dissolved in 5.8 mL of double distilled H_2O . Subsequently, the solutions were mixed together and stirred for next 1 h. The resulting solution was transported to an autoclave and hydrothermal treated at 423 K for 24 h. After the aging period and quenching (fast cooling) of the autoclave, the uniform, milk-like suspension, containing Beta nanoparticles with the Si/Al ratio of 21, was obtained.

In the first synthesis route (impregnation method), the prepared earlier SBA-15 mesoporous silica material (synthesis details presented in [35]), was impregnated with Beta nanoparticles slurry using wet method. 15 mL of the nanoparticles suspension per one gram of SBA-15 was used. The first sample was impregnated with the as-prepared nanoparticle slurry (Beta/SBA-15) and another one with the acidified suspension (Beta(A)/SBA-15). The acidification of the Beta zeolite nanoparticles (5 mL of concentrated HCl per 18 mL of the nanoseeds slurry) resulted in the limitation of the zeolite crystals growth. The impregnated samples were dried in ambient conditions and calcined at 823 K for 6 h.

In the second synthesis route (non-templating method), nanoparticles of Beta zeolite were acidified using the same nanoseeds/HCl ratio as in case of the previous synthesis. The protonated nanocrystals were transferred into the autoclave and hydrothermally treated at 423 K for 72 h. After aging and quenching of the autoclave, a resulting white, gel-like product (Beta/meso) was washed (3 times with 25 mL of double distilled H_2O), dried in ambient conditions and calcined at 823 K for 6 h.

Beta zeolite, obtained by hydrothermal treatment of the parent solution (the same as for the preparation of Beta zeolite nanoparticles) at 423 K for 8 days, was used as a reference sample. After aging and quenching of the autoclave, a resulting white solid product (Beta) was filtered, washed (3 times with 25 mL of double distilled H_2O), dried in ambient conditions and calcined at 823 K for 6 h.

The Na-forms of the obtained samples (codes are given in Table 1) were double exchanged with a solution of NH_4NO_3 (0.5 M, Sigma–Aldrich) at 353 K for 1 h, filtered, washed (3 times with 25 mL of double distilled H_2O), dried in ambient conditions. Finally, the samples were calcined at 823 K for 6 h to convert them to H-forms.

In the next step, iron was introduced to the samples by ion-exchange method, using 0.06 M solution of $\text{FeSO}_4 \cdot 7\text{H}_2\text{O}$ (Sigma–Aldrich). Ion exchange was performed for 6 h at 358 K in anaerobic atmosphere to avoid oxidation of Fe^{2+} to Fe^{3+} (Fe^{3+} easily aggregate to Fe_2O_3 phase, which is known to be catalytically inactive in N_2O decomposition). Then the samples were filtered, washed (3 times with 25 mL of double distilled H_2O), dried in ambient conditions and calcined at 823 K for 6 h.

2.2. Catalysts characterization

The low-temperature nitrogen adsorption–desorption measurements were performed using an ASAP 2010 Micromeritics instrument. Prior to the nitrogen adsorption at 77 K the samples

Table 1
Conditions of N₂O decomposition over Fe-Beta/meso.

Inlet composition	Total flow (ml/min)	w/n _{N₂O} (g h/mol)	C _{N₂O} (ppm)	C _{O₂} (ppm)	C _{CO} (ppm)	C _{H₂O} (ppm)	C _{NO} (ppm)
N ₂ O	50	149	5000	–	–	–	–
N ₂ O + O ₂	50	149	5000	45,000	–	–	–
N ₂ O + O ₂ + H ₂ O	50	149	5000	45,000	–	30,000	–
N ₂ O + O ₂ + H ₂ O + NO	50	149	5000	45,000	–	30,000	200
N ₂ O + CO	50	149	5000	–	5000	–	–
N ₂ O + CO + O ₂	50	149	5000	45,000	5000	–	–
N ₂ O + CO + O ₂ + H ₂ O	50	149	5000	45,000	5000	30,000	–

were outgassed under vacuum at 623 K for 12 h. The specific surface area of the obtained micro-mesoporous materials and the reference samples was determined using BET (Braunauer–Emmett–Teller) model. The micropore volume was calculated using t-plot analysis and the total pore volume was determined at P/P_0 of 0.99.

The X-ray diffraction (XRD) patterns of the samples were recorded using a Bruker D2 Phaser instrument. The measurements were performed in the 2 theta range of 5–60° and additionally, for SBA-15 in the range of 0.5–10° with a step of 0.02°.

Thermogravimetric measurements were performed using a TGA/SDTA851^e Mettler Toledo instrument. The experiments were performed in a flow of synthetic air (80 mL/min) in the temperature range of 303–1073 K, at a heating rate of 10 K/min.

IR measurements were performed using a Nicolet 6700 FT-IR spectrometer (Thermo Scientific) equipped with DRIFT (diffuse reflectance infrared Fourier transform) accessory and DTGS detector. The dried samples were grounded with a dried potassium bromide powder (4 wt.%). The measurements were carried out in the wavenumber range of 400–4000 cm^{−1} with a resolution of 2 cm^{−1}.

Iron content in the catalysts was calculated from the difference in iron content in solutions used in ion-exchange method—before and after iron deposition. The analyses were performed using a Thermo Scientific Evolution 220 UV-Visible spectrometer. The absorbance of Fe(II) complex with 1,10-phenanthroline was measured at 512 nm.

Coordination and aggregation of iron species introduced into the obtained materials were studied by UV-vis-DR spectroscopy. The measurements were performed using an Evolution 600 (Thermo) spectrophotometer in the range of 200–900 nm with a resolution of 2 nm.

All X-band CW-EPR spectra have been recorded at liquid nitrogen temperature (77 K) with a Bruker ELEXSYS E-500 spectrometer, operating at a 100 kHz field modulation. The intensities of the corresponding signals have been expressed by the values of their double integrals.

The STEM images were obtained with the use of a Tecnai Osiris 200 kV TEM/STEM system equipped with HAADF detector and Super-EDX windowless detector. STEM micrographs (512 × 512 points) were coupled with EDX data for the presentation of the chosen elements distribution.

2.3. Catalytic tests

Catalytic studies of N₂O decomposition in the presence of oxygen were performed in a fixed-bed quartz microreactor. The experiments were done at atmospheric pressure and in the temperature range from 423 to 823 K in intervals of 50 K. The composition of outlet gases was analyzed using a gas chromatograph (SRI 8610C) equipped with TCD detector. For each experiment 0.1 g of catalyst (particles sizes in the range of 0.160–0.315 mm) was placed on quartz wool plug in the reactor and outgassed in a flow of pure helium at 823 K for 1 h. Then the gas mixture containing 5000 ppm of N₂O and 45,000 ppm of O₂ diluted in pure helium (total flow rate of 50 ml/min) passed over the catalyst and the reaction

proceeded for about 4 h to stabilize the catalyst. The space time (τ) of N₂O in these conditions, defined as $\tau = W/n_{N_2O}$ (where: W is a catalyst mass, and is a n_{N_2O} molar flow of N₂O in the inlet mixture) was equal to 149 g h mol^{−1}. The analysis of the outlet gases was performed 20 min after the temperature stabilization and a steady state regime was achieved.

Additionally, for the selected sample, an influence of various gases (O₂, H₂O, NO) on efficiency of N₂O decomposition and reduction by CO were studied. The compositions of the reaction mixtures are summarized in Table 1. Analysis of nitrous oxide and products of its decomposition was performed by a quadrupole mass spectrometer RGA 200 (Prevac), while the reactants and all possible products of N₂O reduction by CO were analyzed by a gas chromatograph YL6100GC (equipped with HP-PLOT/Q and GsBP-PLOT columns and TCD detector).

3. Results and discussion

The textural parameters of SBA-15 mesoporous silica, Beta zeolite and hierarchical micro-mesoporous samples, determined by nitrogen sorption measurements, are presented in Table 2. Deposition of Beta zeolite nanoparticles on SBA-15 resulted in a decrease in its total surface area as well as volume and surface area of mesopores. It could be explained by partial blocking of the mesopore channels in SBA-15 by zeolite nanoparticles. On the other hand, after impregnation micropore volume in the samples increased, what indicates the successful introduction of the zeolite phase into SBA-15 support. These tendencies were observed for SBA-15 impregnated with acidified and non-acidified zeolite nanoparticles.

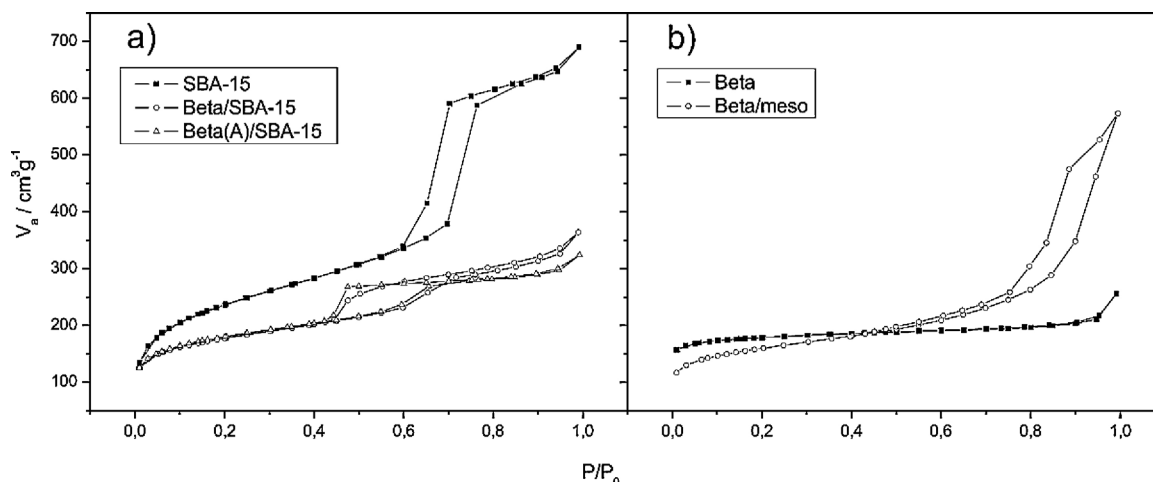
A second series of the samples was obtained by non-templating method. In this case mesoporous material was composed of aggregated Beta nanoparticles and was characterized by lower surface area and micropore volume in comparison to classical, microporous zeolite (Beta). These differences could be explained by various duration of the crystallization process for both zeolitic samples. On the other hand, the volume and surface area of mesopores determined for the Beta/meso sample were higher than for conventional Beta zeolite, what proves the successful generation of mesopores in this material.

The nitrogen adsorption–desorption isotherms of micro-mesoporous materials and reference samples are shown in Fig. 1. The isotherms, which can be classified as type IV (IUPAC), were recorded for SBA-15, non-modified and impregnated with Beta nanoparticles, proved the presence of mesopores in these samples (Fig. 1a). In case of SBA-15, the hysteresis loop is type of H1, characteristic for the narrow distribution of cylindrical and both sides opened mesopores, was recorded. Deposition of Beta zeolite nanoparticles (Beta/SBA-15, Beta(A)/SBA-15) resulted in the modification of the hysteresis profile, which could be classified as H2 type (ink bottle like pores) pointing the location of the zeolite particles at the entrances of mesopores.

The isotherm of type I (according to the IUPAC classification), characteristic of microporous structure, was obtained for Beta zeolite (Fig. 1b). In case of the Beta/meso sample an increase of the nitrogen adsorbed volume, observed in the range of low partial

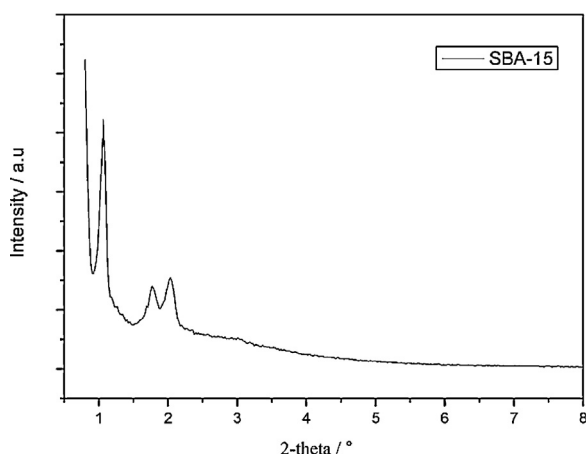
Table 2Textural properties of the samples determined from N₂-sorption measurements at 77 K.

Sample code	S_{BET} (m ² /g)	Micropore volume (cm ³ /g)	Mesopore volume (cm ³ /g)	Mesopore area (m ² /g)
SBA-15	809	0.118	0.949	567
Beta/SBA-15	579	0.146	0.417	293
Beta(A)/SBA-15	586	0.154	0.347	284
Beta	546	0.238	0.158	88
Beta/meso	519	0.135	0.752	258

**Fig. 1.** Nitrogen adsorption-desorption isotherms recorded at 77 K, for (a) blank SBA-15 and its modifications with deposited Beta nanoparticles, (b) conventional and mesoporous Beta zeolites.

pressures, is smaller than for the Beta sample. It could be explained by a shorter crystallization time of Beta/meso. Additionally, the isotherm recorded for this sample possesses the hysteresis loop of type H3 in the range of higher nitrogen partial pressures, related to the presence of mesopores. The differences between isotherms obtained for classical (Beta) and mesoporous (Beta/meso) zeolites indicate the formation of mesopores between the aged Beta zeolite nanoparticles.

X-ray diffraction method was used for determination of the porous structure of SBA-15 [35] (Fig. 2) and to investigate the presence of the crystalline zeolite phase in the Beta/SBA-15, Beta(A)/SBA-15, Beta/meso and Beta samples (Fig. 3). The reflections identified in the low 2θ angel range ($d_{100}=9.2$ nm, $d_{110}=5.0$ nm and $d_{200}=4.4$ nm) confirmed the 2D hexagonally structured pore system of SBA-15. Reflections in the higher 2θ angle

**Fig. 2.** XRD pattern of the SBA-15 mesoporous sample.

range were not observed due to the amorphous structure of pore walls.

Reflections at 2θ about 6.5–8.5° and 20–25°, characteristic of Beta zeolite, appeared after impregnation of SBA-15 with Beta zeolite nanoparticles. These reflections proved the presence of the zeolite phase in the obtained samples. The intensity of these reflections is significantly lower in comparison to conventional Beta zeolite. Additionally, an increase in intensity of the broad signal, spread in the range 2θ of about 15–35° and associated with the presence of amorphous silica, were observed for the samples with decreasing content of the zeolitic phase. Thus, it could be concluded that the content of the zeolitic phase in the impregnated samples is relatively small. The intensity of the reflections characteristics of Beta zeolite is slightly higher in case of the Beta/SBA-15 sample in comparison to Beta(A)/SBA-15, in which case the growth of the zeolite crystals was stopped by acidification of the zeolite nanoparticles slurry.

The reflections characteristic of Beta zeolite were identified in diffraction pattern of the Beta/meso sample. The content of the zeolite phase in this sample is smaller than in case of Beta zeolite, but higher than for the impregnated samples (Beta/SBA-15 and Beta(A)/SBA-15).

The contribution of the zeolite phases in the combined micro-mesoporous materials can be also analyzed by thermal analysis of the as-prepared, non-calcined samples. The DTG profiles of the micro-mesoporous samples and, for comparison, also Beta zeolite are presented in Fig. 4. DTG curve obtained for Beta zeolite consists of four steps of weight loss. The first, observed at temperature below 423 K, is assigned to desorption of zeolitic water, while the second (423–623 K) and the third (623–773 K) ones are related to evacuation of TEA⁺ cations balancing the negative charge of lattice aluminum occluded in the zeolite framework or interacting with the zeolite framework. The fourth region, above 773 K, corresponds to the burning of the residual organic templates [36,37].

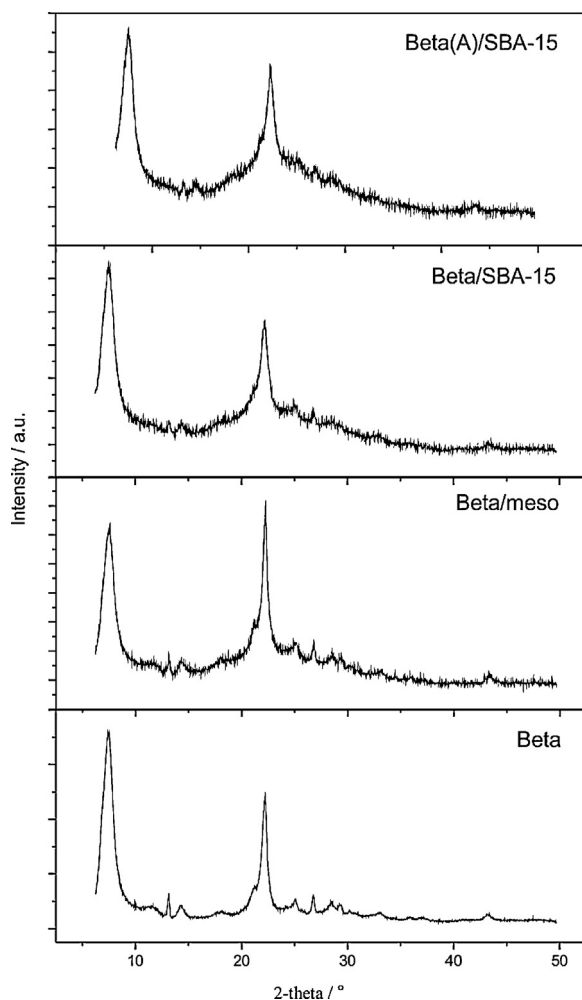


Fig. 3. XRD patterns of Beta zeolite and micro-mesoporous samples.

The DTG curves of the obtained micro-mesoporous materials contain four regions of weight loss, characteristic of Beta zeolite, however there is a significant difference between them. For the micro-mesoporous samples (Beta/SBA-15, Beta(A)/SBA-15 and Beta/meso), weight loss observed in the second region is more intensive than for Beta zeolite. However, weight loss determined for the third step is more intensive for Beta zeolite. These differences could be related to shorter crystallization time of the zeolite phase in case of the micro-mesoporous samples. It resulted in a lower content of TEA^+ built in the zeolite structure and therefore, their weaker stabilization in the pore system.

DRIFT spectra, recorded for Beta zeolite and the micro-mesoporous samples (Beta/SBA-15, Beta(A)/SBA-15 and Beta/meso) in the range from 400 to 2000 cm^{-1} , are shown in Fig. 5. The absorption bands at 525 and 575 cm^{-1} are related to the presence of five and six membered rings characteristic for the Beta zeolite structure. Such bands are present in the spectra of the micro-mesoporous samples, however their intensities are lower than in the spectrum of Beta zeolite. It could be explained by lower content of the zeolitic phase in the micro-mesoporous samples (Beta/SBA-15, Beta(A)/SBA-15 and Beta/meso). For Beta(A)/SBA-15 the intensity of these bands is lower than for the sample produced using the as-prepared Beta nanoparticles (Beta/SBA-15).

Additionally, the intensity of band located at 1230 cm^{-1} , attributed to the asymmetric stretching of strained siloxane bridges (with the same bond length) present in the zeolite pore walls [34],

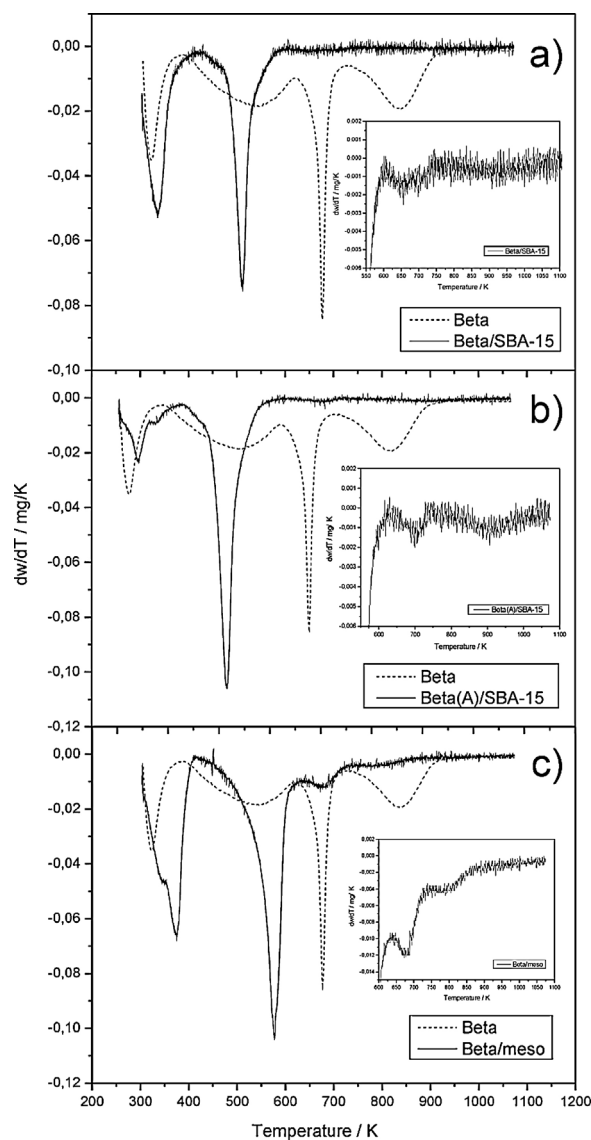


Fig. 4. DTG profiles of Beta/SBA-15 (a), Beta(A)/SBA-15 (b) and Beta/meso (c) samples compared with Beta zeolite.

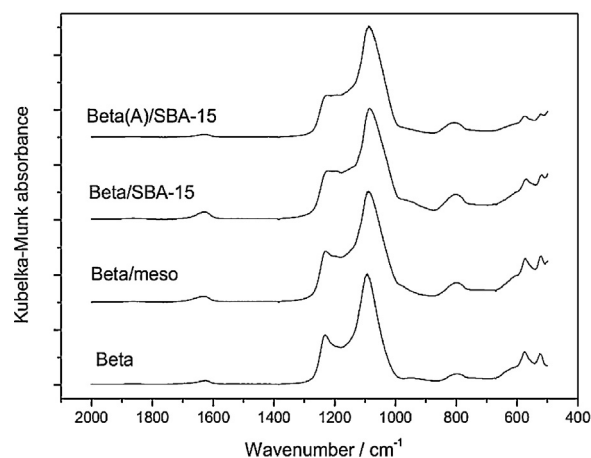


Fig. 5. DRIFT spectra of Beta zeolite and micro-mesoporous samples.

changed proportionally to the content of the zeolite phase in a series of spectra recorded for the micro-mesoporous materials.

The content of iron introduced to the samples by ion-exchange method is presented in Table 3. The lowest loading of iron was measured for the Fe-SBA-15 sample. It could be explained by an amorphous nature of SBA-15 material without any ion-exchange properties. On the other side, the highest amount of iron was introduced to the Fe-Beta sample, which possess the strongest, among the examined samples, zeolitic character and therefore, the highest ion-exchange capacity. In case of micro-mesoporous materials the content of iron depended on the crystallization time of Beta seeds (zeolitic phase content) and is as follows: Fe-Beta/meso > Fe-Beta/SBA-15 > Fe-Beta(A)/SBA-15. The impregnation of SBA-15 with Beta nanoparticles resulted in generation of ion-exchange properties and therefore, the introduction of larger amount of iron was possible. Acidification of the zeolite nanoparticles slurry stopped the zeolite crystals growth, decreasing a number of ion-exchange positions and thereby lower amount of iron, in comparison to the sample impregnated without acidification, was introduced.

Diffuse-reflectance UV-vis spectroscopy was used to determine the nature and distribution of iron species, introduced Beta zeolite, SBA-15 and micro-mesoporous samples (Fig. 6).

The bands characteristic of iron species can be expected in three regions of UV-vis-DR spectra. Absorption below 300 nm is attributed to the presence of isolated Fe^{3+} ions (215 and 285 nm in tetrahedral and octahedral coordination, respectively). Bands, located in the range of 300–400 nm, are related to the presence of small oligonuclear $\text{Fe}_x^{3+}\text{O}_y$ clusters, while adsorption above 400 nm is attributed to the presence of bulky Fe_2O_3 crystallites located probably on the external surface of the zeolite crystals [10,38].

In case of Fe-SBA-15 only one band, located at about 250 nm, was detected. In this case the mechanism of iron deposition is based on the weak Van der Waals interactions of Fe cations with amorphous walls of SBA-15. Due to the presence of mesopores the mobility iron species through the channels in this material is undisturbed and iron was deposited only in the form of isolated Fe^{3+} ions.

Three bands, characteristic for Fe^{3+} ions in the form of isolated cations, oligomeric $\text{Fe}_x^{3+}\text{O}_y$ and bulky Fe_2O_3 clusters, were found in a spectrum obtained for the Fe-Beta sample. The presence of the aggregated Fe-species could be a result of the limited mobility of iron ions in the micropore system of this sample. The presence of bulky iron oxide on the catalyst surface is not preferred from the point of view of its application in the N_2O decomposition processes, in which Fe_2O_3 was found to be inactive [39].

The shape of the spectra obtained for micro-mesoporous materials is significantly different from the spectrum of Fe-Beta. The band at about 500 nm, related to the presence of clustered Fe_2O_3 significantly decreased, while the absorption related to isolated Fe^{3+} ions increased. This change could be explained by better accessibility of the ion-exchange positions in the zeolitic phase dispersed among the combined porous materials.

The differences between the spectra of Fe-Beta/SBA-15 and Fe-Beta(A)/SBA-15 could be caused by various size of the zeolite Beta crystals (acidification of the Beta seeds slurry in case of Fe-Beta(A)/SBA-15 stopped the crystals growth). It cannot be also excluded that smaller zeolite crystallites were deposited in less accessible positions in the SBA-15 structure, thereby the ion exchange positions were blocked.

The EPR spectroscopy was another method used for identification of iron species in the samples (Fig. 7). The EPR signals at $g \approx 4.3$ and 2.0 ascribed to the high-spin $3d^5 \text{Fe}^{3+}$ ($S = 5/2$) ions, were distinctly observed in all recorded spectra. Any strong qualitative differences can be observed, reflecting quite similar status of Fe^{3+} ions in all investigated samples, except of the case of

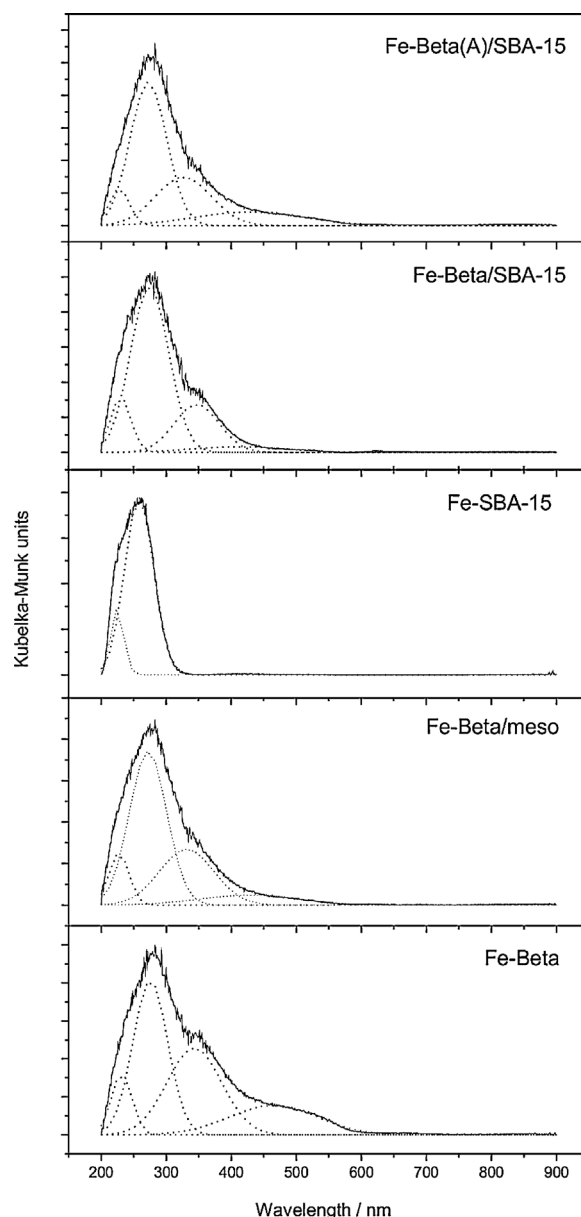


Fig. 6. UV-vis-DR spectra of iron exchanged Beta zeolite, SBA-15 and micro-mesoporous samples.

Fe-Beta/SBA15, where a weaker broad signal at $g \approx 2.4$ can additionally be identified.

As it can be inferred from the EPR results, the majority of Fe^{3+} ions is magnetically isolated and locally stabilized in oxygen surrounding. The strong characteristic signal around $g \approx 4.3$ is typical of Fe^{3+} centers in rhombically distorted environment (ZFS parameters $|E/D| = 1/3$), whereas the narrow one at $g \approx 2.0$ can be attributed to the Fe^{3+} ions occupying the sites of higher symmetry ($E \approx 0$) [40,41].

Both the framework and extraframework Fe^{3+} ions of tetrahedral (or higher) coordination can give rise to the signal at $g \approx 4.3$. In turn, the line at $g \approx 2.0$ can be attributed to the octahedrally-coordinated Fe^{3+} ions isolated in extraframework iron oxide clusters [5,42]. The broader signal around $g \approx 2.4$, can be assigned to the presence of small iron clusters (oligomeric Fe_xO_y species), in which Fe^{3+} ions can interact magnetically, that enables Heisenberg-type exchange interactions [43]. The highest contribution of the signal at $g \approx 2.4$ to the corresponding EPR

Table 3
Iron content in the samples.

Sample code	Fe-SBA-15	Fe-Beta/SBA-15	Fe-Beta(A)/SBA-15	Fe-Beta	Fe-Beta/meso
Fe content/%	0.06	0.51	0.49	3.54	1.26

spectrum was observed for the Fe-Beta/SBA15 sample. It is consistent with the results of UV–vis-DRS studies, which showed the highest contribution of oligomeric iron oxide species in this sample.

Analyzing the differences in the values of the integral intensity ratios determined from the EPR lines observed at $g \approx 4.3$ and 2.0 ($I_{4.3}/I_{2.0}$), it can be noted that for almost all investigated cases, except of the Fe-Beta/SBA15 sample, the $I_{4.3}/I_{2.0}$ ratio ranges from ca. 1.27 (for Fe-Beta), ca. 1.32 (for Fe-Beta/meso) to ca. 1.38 (for Fe-Beta(A)/SBA15), reflecting the preferential stabilization of Fe^{3+} ions in rhombically distorted environment. Contrary to this, in case of the Fe-Beta/SBA15 sample, the determined $I_{4.3}/I_{2.0}$ intensity ratio was distinctly lower and equal to ca. 0.85. It should be however kept in mind that in this particular case the broad signal at $g \approx 2.4$ attributed to the small oligomeric Fe_xO_y species contributed to the corresponding EPR spectrum. This means that in such a case the amount of Fe^{3+} ions occurring in small clusters increased mainly on the expense of the Fe^{3+} ions isolated in rhombically distorted surrounding. Of course, a certain amount of oxide like species, containing octahedrally coordinated Fe^{3+} , can be reduced in this case as it can be inferred from the shape of the corresponding EPR spectrum.

Various micro-mesopore structures of the samples influenced the form and aggregation of deposited iron species. As it was found out from the EPR analysis, the content of monomeric Fe^{3+} ions and oligomeric Fe_xO_y species is higher in Fe-Beta/meso and Fe-Beta/SBA-15 comparing to that determined in conventional Fe-Beta zeolite. On the other hand the Fe-Beta sample contains more extraframework iron oxide clusters. The preferential formation of monomeric and oligomeric iron species in the combined micro-mesoporous materials could be related to the better accessibility of ion-exchange positions in the zeolitic phase. Acidification of Beta zeolitic seeds (Fe-Beta(A)/SBA15) strongly increased the population of iron oxide clusters in the sample. Thus, it cannot be excluded, that this phenomenon is related to different location of zeolitic seeds in the SBA-15 structure. It seems possible that smaller zeolite seeds, formed in the acidified sample (Fe-Beta(A)/SBA15), were deposited in the less accessible regions of the SBA-15 porous structure, possibly inside of the channels. In consequence, the ion exchange positions were sterically blocked. Thus, the mobility of iron species in the pore system was limited in comparison to that occurring in the non-acidified sample (Fe-Beta/SBA-15), where the content of oligomeric and isolated iron species was distinctly higher.

STEM images (Fig. 8) of the selected iron-exchanged samples (Fe-Beta, Fe-Beta/meso and Fe-Beta(A)/SBA-15) give an overview of the combined micro-mesoporous materials arrangement. The morphology of the Fe-Beta/meso sample differs significantly from the structure of the Fe-Beta sample. Acidified zeolite Beta seeds, subsequently aged under hydrothermal conditions, aggregated with the formation of the much more loose structure in comparison to conventional Beta zeolite (Fig. 8b). The mesoporosity in the Fe-Beta/meso sample was generated between the zeolitic seeds of the size of 10–20 nm. In case of the Fe-Beta(A)/SBA-15 image (Fig. 8c) the uniform parallel mesopores of SBA-15 (size of about 10 nm) are visible. The acidified Beta seeds (size of about 5 nm) introduced by wet impregnation were deposited on the external surface and inside of SBA-15 mesopores.

Distribution of aluminum (component of the zeolitic phase) and iron was determined by EDX measurements. The uniform aluminum distribution does not fully coincide with iron dispersion in the Fe-Beta sample (Fig. 8a). In this case, apart from well dispersed iron species, also Fe_2O_3 clusters located on the sample surface, were found. Concentration of aluminum in both micro-mesoporous samples (Fe-Beta/meso and Fe-Beta(A)/SBA-15), evaluated from the EDX analysis, is smaller in comparison to conventional Fe-Beta zeolite. It could be explain by a shorter crystallization time (smaller content of the zeolitic phase). However, the uniform distribution of aluminum proves the zeolitic character of Fe-Beta/meso as well as a homogenous scattering of zeolitic seeds in Fe-Beta(A)/SBA-15. Uniform distribution of iron was found in Fe-Beta/meso. While for the impregnated sample also Fe_2O_3 clusters were identified. These results are fully supported by UV–vis-DRS and EPR measurements.

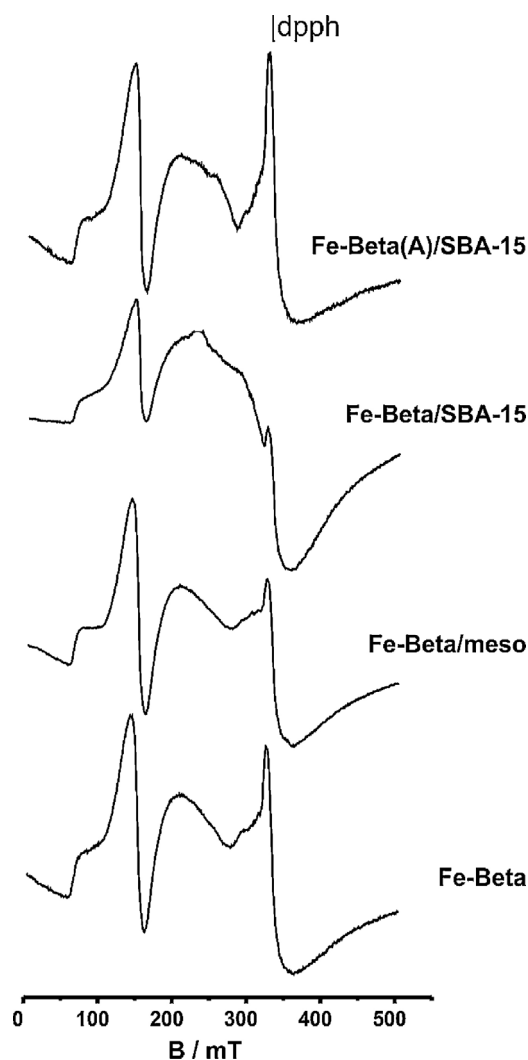


Fig. 7. EPR spectra of iron exchanged Beta zeolite, SBA-15 and micro-mesoporous samples.

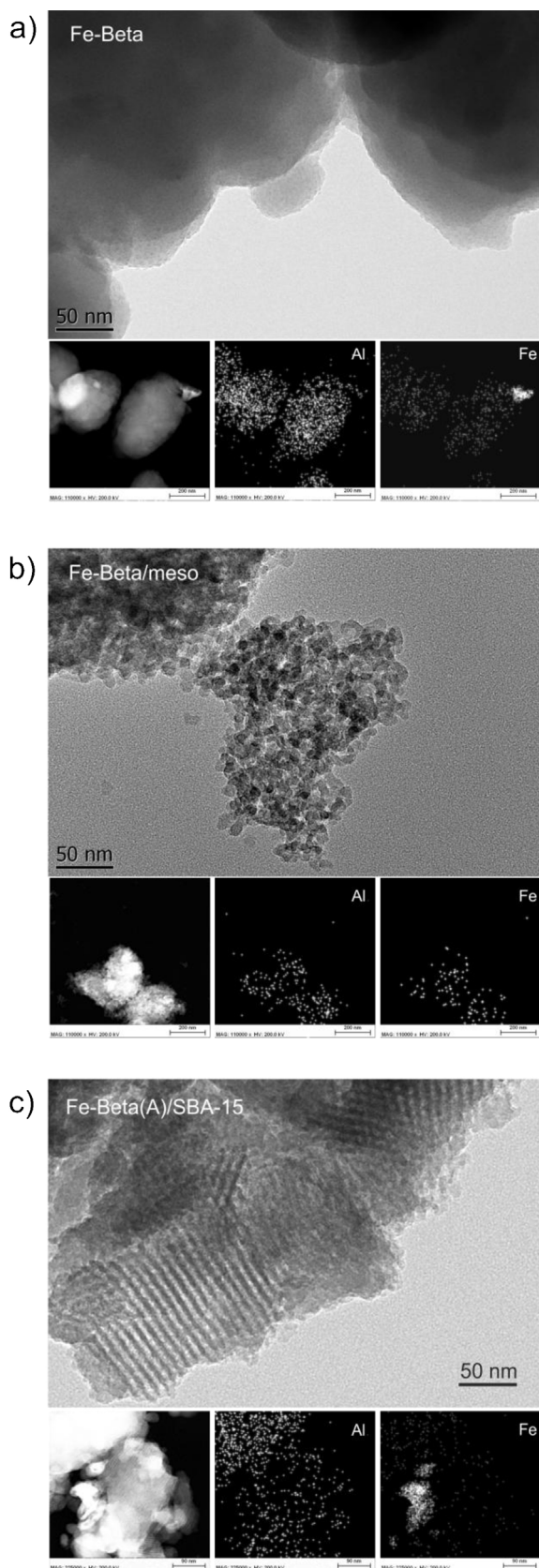


Fig. 8. STEM images and EDX analysis of Fe-Beta (a), Fe-Beta/meso (b) and Fe-Beta(A)/SBA-15 (c) samples.

Fe-exchanged SBA-15, Beta zeolite and micro-mesoporous materials with the zeolitic properties were tested as catalysts for N_2O decomposition in the presence of oxygen (Fig. 9a).

The results, obtained for the synthesized samples, were compared with those measured for commercial Beta zeolite supplied by Zeolyst ($\text{SiO}_2/\text{Al}_2\text{O}_3 = 38$, $S_{\text{BET}} = 710 \text{ m}^2/\text{g}$). Commercial zeolite was modified with iron using the same procedure as for the described above catalysts. This reference sample was denoted as Fe-Beta(Zeolyst).

The Fe-SBA-15 sample was found to be catalytically inactive in the studied temperature range. However, deposition of Beta zeolite nanoparticles on SBA-15 followed by the iron-exchange (Fe-Beta/SBA-15 and Fe-Beta(A)/SBA-15) resulted in a significant increase in its catalytic activity. The N_2O conversion over Fe-Beta/SBA-15 is shifted by about 20 K into the lower temperatures in comparison to the sample impregnated with acidified nanoseeds (Fe-Beta(A)/SBA-15). This dissimilarity is probably related to the stronger zeolitic character (higher crystallinity) of the Fe-Beta/SBA-15 sample and differences in the forms of introduced iron species.

The N_2O conversion profiles obtained for synthesized Fe-Beta and commercial Fe-Beta (Zeolyst) are similar. The only small differences, observed in the conversion profiles, could be related to the various Si/Al ratios and different surface areas of the samples. The Fe-Beta and Fe-Beta/meso samples were found to be the most active catalysts among the synthesized samples. Complete N_2O conversion over these catalysts was achieved at 773 K. Small differences in the N_2O conversion profiles, observed for these catalysts at lower temperatures, could be explained by lower content of the catalytically active zeolitic phase in the Fe-Beta/meso sample.

Because the micro-mesoporous catalysts differ in the specific surface area as well as iron content and distribution of various forms of this metal, therefore the results of the catalytic experiments were also presented as a specific reaction rate related to iron content (Fig. 9b). Analysis of these results showed that the most catalytically active iron centres are present in the impregnated samples (Fe-Beta/SBA-15, Fe-Beta(A)/SBA-15). Less active iron species are present in the sample obtained by non-templating method (Fe-Beta/meso). It should be noted that iron species found in all micro-mesoporous samples are more active than those in conventional Fe-Beta zeolite. Comparison of the results of the catalytic studies (Fig. 9b) and spectroscopic methods (UV-vis-DRS and EPR) used for determination of the iron species forms introduced to the samples showed that this metal was present in Fe-Beta/SBA-15 nearly exclusively in the form of isolated Fe^{3+} cations and small $\text{Fe}_x^{3+}\text{O}_y$ oligomers. For the samples, presenting lower reaction rate (Fe-Beta(A)/SBA-15 and Fe-Beta/meso), additionally bulky iron oxide was identified. While for Fe-Beta, which presented the lowest reaction rate related to iron content (Fig. 9b), the intensity of the band characteristic of bulky Fe_2O_3 clusters was the most intensive in a series of the studied samples. Thus, it could be concluded that iron in the form of well dispersed species (monomeric Fe^{3+} cations and small $\text{Fe}_x^{3+}\text{O}_y$ oligomers) is much more catalytically active than aggregated, bulky iron oxide clusters. Such dispersed forms, especially oligomeric iron oxide species, were reported to contain so called α -sites (binuclear Fe^{2+} complexes), catalytically active in N_2O decomposition [44,45]. Such α -sites are able to effectively decompose nitrous oxide via the $\text{Fe}^{2+} \rightarrow \text{Fe}^{3+}$ transition and generation of α -oxygen (paired oxygen atoms, each bonded to one Fe site in ferryl groups).

The most active catalyst (Fe-Beta/meso) was tested in N_2O decomposition and reduction using reaction mixtures containing various components (Table 1, Fig. 10): (i) N_2O , (ii) $\text{N}_2\text{O} + \text{O}_2$, (iii) $\text{N}_2\text{O} + \text{O}_2 + \text{H}_2\text{O}$, (iv) $\text{N}_2\text{O} + \text{O}_2 + \text{H}_2\text{O} + \text{NO}$, (v) $\text{N}_2\text{O} + \text{CO}$, (vi) $\text{N}_2\text{O} + \text{CO} + \text{O}_2$, (vii) $\text{N}_2\text{O} + \text{CO} + \text{O}_2 + \text{H}_2\text{O}$.

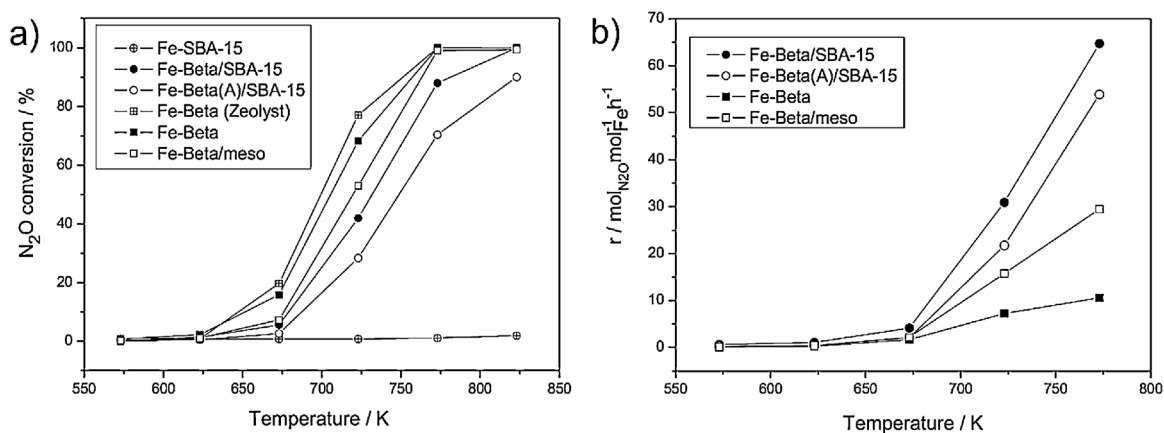


Fig. 9. Temperature dependence of N_2O conversion (a) and specific reaction rate (b) for iron-exchanged Beta zeolite, SBA-15 and micro-mesoporous samples. Conditions: 5000 ppm N_2O , 45,000 ppm O_2 , He as balancing gas; total flow rate – 50 ml/min; weight of catalyst – 0.1 g.

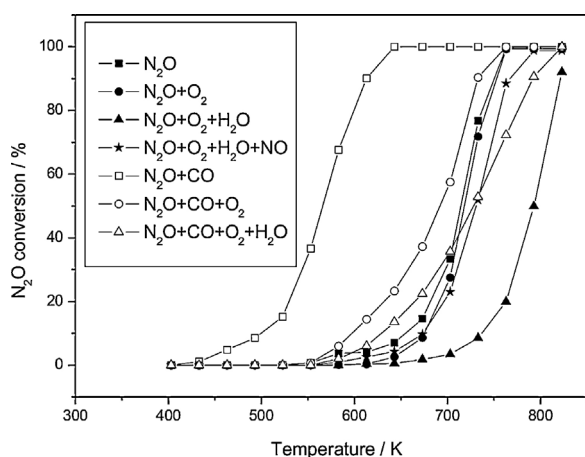


Fig. 10. Temperature dependence of N_2O conversion for Fe-Beta/meso in the presence of different compositions of reaction mixture. Conditions: 5000 ppm N_2O and optionally: 45,000 ppm O_2 , 30,000 ppm H_2O , 200 ppm NO, 5000 ppm CO; He as balancing gas; total flow rate – 50 ml/min; weight of catalyst – 0.1 g.

As it can be seen from Fig. 10, the presence of oxygen has a small impact on the N_2O conversion. It means that the contribution of elementary steps involving oxygen adsorption (Eq. (1)) and dissociation (Eq. (2)) on active centers in the N_2O decomposition mechanism, is negligible [3,46].

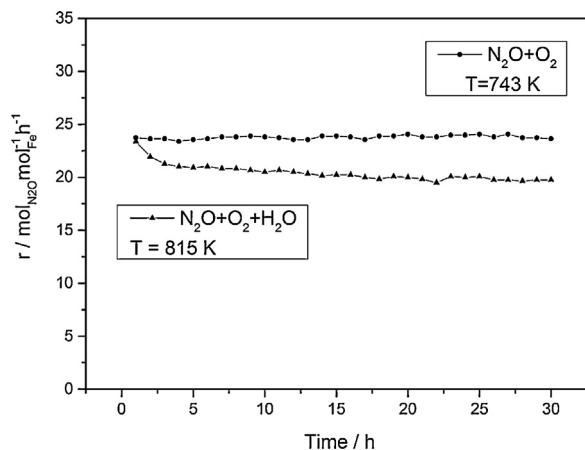


Fig. 11. Stability tests (30 h) of Fe-Beta/meso in a flow of the reaction mixtures containing (i) 5000 ppm N_2O , 45,000 ppm O_2 , He as balancing gas; (ii) 5000 ppm N_2O , 45,000 ppm O_2 , 30,000 ppm H_2O , He as balancing gas.

The presence of water significantly decreases the N_2O conversion. H_2O molecules act as the catalyst poison occupying the active centers and therefore, making them unavailable for N_2O chemisorption.

The presence of NO significantly increased the N_2O conversion. Despite simultaneous presence of H_2O and NO, the activity of the catalyst was close to that measured in the inert conditions. This result proves that the role of NO is purely catalytic and it acts as an intermediate oxygen storage (so called O_2 desorption-accelerator). Nitric oxide is expected to adsorb on the catalyst surface and react with chemisorbed oxygen atom (product of N_2O decomposition, Eq. 3) with the formation of NO_2 . Thus, the active site is liberated and ready for the oxygen bounding from next N_2O molecule (Eq. (4)–(7)) [47–50].

Adsorbed oxygen (product of N_2O decomposition) can be easily removed from the catalyst surface by the reaction with CO. The redox (Eq. (3), (8)–(10)) and associative (Eq. (11)–(14)) mechanisms have been proposed to describe the CO role in the reaction system [51]. It is worth to mention that the N_2O conversion with CO, is more effective than N_2O decomposition in inert gas flow (shifted by about 120 K). CO, in the presence of oxygen, acts as a non-selective reductant thereby inhibiting the N_2O conversion rate. High activity of catalyst in nitrous oxide reduction by CO could be an interesting issue in elimination of N_2O from waste gases emitted by oxalic acid plants, in which carbon monoxide is a typical component.

It should be stressed that, in all the studied reactions, apart from N_2 any other N-containing reaction products were not detected.



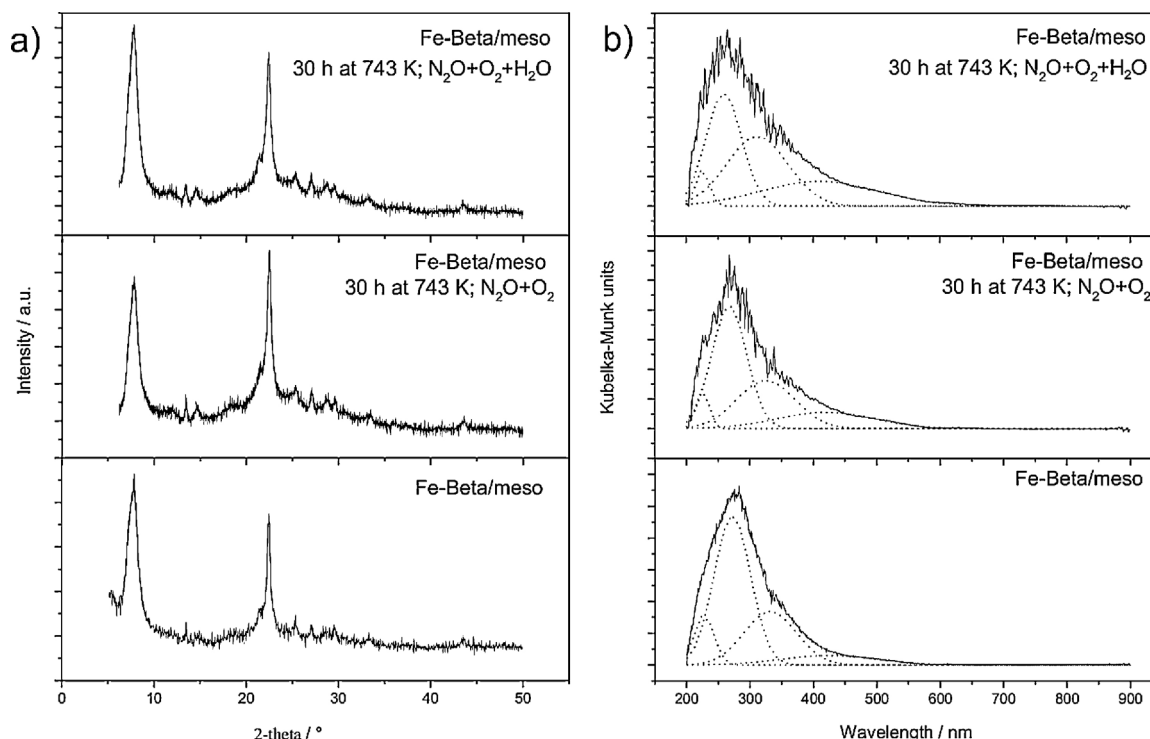


Fig. 12. XRD patterns (a) and UV-vis-DR spectra (b) of Fe-Beta/meso, after stability tests in N_2O decomposition.



For the Fe-Beta/meso catalyst additional stability tests were done. These extended catalytic tests (30 h time on stream) were performed in a flow of the following gas mixtures: (i) $N_2O + O_2$, (ii) $N_2O + O_2 + H_2O$. These tests were performed at temperatures necessary to obtain about 80% of N_2O conversion (743 and 815 K, respectively for the tests with dry and wet reaction mixture). Results of the stability tests are presented in Fig. 11. Any significant changes in the reaction rate were observed during the stability test performed in a flow of the oxygen containing reaction mixture (dry mixture). While, for the test with the wet, oxygen containing reaction mixture, the reaction rate decreased by about 10% during first four hours and then reached the nearly constant level, which was stable to the end of the test.

After stability tests, the Fe-Beta/meso samples were analyzed with respect to the textural properties (low temperature N_2 adsorption), crystalline structure (XRD) and forms of iron species (UV-vis-DRS). Surface area, micro and mesopore volumes measured for the Fe-Beta/meso samples after stability tests in dry ($S_{BET} = 458 \text{ m}^2/\text{g}$, $V_{micro} = 0.112 \text{ cm}^3/\text{g}$, $V_{mezo} = 0.669 \text{ cm}^3/\text{g}$) and wet conditions ($S_{BET} = 525 \text{ m}^2/\text{g}$, $V_{micro} = 0.124 \text{ cm}^3/\text{g}$, $V_{mezo} = 0.571 \text{ cm}^3/\text{g}$) do not differ significantly from the textural parameters of the parent micro-mesoporous sample. Neither the high temperature nor the presence of gas mixture containing N_2O , O_2 and H_2O did not change the crystalline structure of Beta zeolite during 30 h of the catalytic test (Fig. 12a). However, these

conditions slightly influenced the form of iron in the samples (Fig. 12b). An increase in contribution of aggregated form of iron oxides (oligomeric $Fe_x^{3+}O_y$ and bulky Fe_2O_3 clusters) was observed for the samples used in the stability tests.

4. Conclusions

Two synthesis routes were applied to obtain the micro-mesoporous materials with the properties of Beta zeolite. Both impregnation and non-templating methods resulted in the formation of materials with the hierarchical porous structure. The properties of the Fe-Beta/meso sample, which possess a distinct mesoporous structure, simultaneously preserving the zeolitic character seems to be the most promising for catalysis. The activity of this catalyst in the process of N_2O decomposition is very similar to the activity of Beta zeolite (Fe-Beta), however it should be noted that the content of the zeolite phase as well as iron loading in the Fe-Beta/meso sample is significantly lower. This indicates that the generation of mesopores has a positive influence on the catalytic properties. Additionally, taking into account that the loading of iron in Fe-Beta/meso is significantly lower comparing to Fe-Beta but activity both these catalysts is very similar, it could be concluded that iron species deposited on Fe-Beta/meso are more active in N_2O decomposition than those present in Fe-Beta. Comparison of the results of the catalytic studies and UV-vis-DRS as well as EPR analysis showed that monomeric Fe^{3+} cations and small $Fe_x^{3+}O_y$ oligomers are much more catalytically active in N_2O decomposition than aggregated, bulky iron oxide clusters.

The non-templating method, used for the synthesis of microporous-mesoporous zeolites, is very promising and application of materials obtained by this method is not limited only to the process of N_2O decomposition.

Acknowledgements

M.R. acknowledges the financial support from the International PhD-studies programme at the Faculty of Chemistry Jagiellonian University within the Foundation for Polish Science MPD Programme co-financed by the EU European Regional Development Fund. The research was carried out with the equipment purchased thanks to the financial support of the European Regional Development Fund in the framework of the Polish Innovation Economy Operational Program (contract no. POIG.02.01.00-12-023/08).

References

- [1] W.C. Troglér, *Coordination Chemistry Reviews* 187 (1999) 303–327.
- [2] J. Pérez-Ramírez, F. Kapteijn, K. Schöffel, J.A. Moulijn, *Applied Catalysis B* 44 (2003) 117–151.
- [3] F. Kapteijn, J. Rodríguez-Mirasol, J.A. Moulijn, *Applied Catalysis B* 9 (1996) 25–64.
- [4] A. Corma, *Chemical Reviews* 97 (1997) 2373–2419.
- [5] J. Pérez-Ramírez, J.C. Groen, A. Brückner, M.S. Kumar, U. Bentrup, M.N. Bebbagh, L.A. Villaescusa, *Journal of Catalysis* 232 (2005) 318–334.
- [6] L. Kiwi-Minsker, D.A. Bulushev, A. Renken, *Journal of Catalysis* 219 (2003) 273–285.
- [7] J.-H. Park, J.-H. Choung, I.-S. Nam, S.-W. Ham, *Applied Catalysis B* 78 (2008) 342–354.
- [8] Q. Shen, L. Li, C. He, H. Tian, Z. Hao, Z. Ping Xu, *Applied Catalysis B* 91 (2009) 262–268.
- [9] L. Li, Q. Shen, J. Li, Z. Hao, Z.P. Xu, G.Q.M. Lu, *Applied Catalysis A* 334 (2008) 131–141.
- [10] J.A.Z. Pieterse, S. Booneveld, R.W. van den Brink, *Applied Catalysis B* 51 (2004) 215–228.
- [11] K. Jiřša, J. Nováková, M. Schwarze, A. Vondrová, S. Sklenák, Z. Sobalik, *Journal of Catalysis* 262 (2009) 27–34.
- [12] J. Čejka, *Catalysis Reviews* 49 (2007) 457–509.
- [13] Y. Tao, H. Kanoh, L. Abrams, K. Kaneko, *Chemical Reviews* 106 (2006) 896–910.
- [14] M. Hartmann, *Angewandte Chemie International Edition* 43 (2004) 5880–5882.
- [15] S. van Donk, A.H. Janssen, J.H. Bitter, K.P. de Jong, *Catalysis Reviews* 45 (2003) 297–319.
- [16] J.C. Groen, L.A.A. Peffer, J.A. Moulijn, J. Pérez-Ramírez, *Colloids and Surfaces A* 241 (2004) 53–58.
- [17] J.C. Groen, L.A.A. Peffer, J.A. Moulijn, J. Pérez-Ramírez, *Chemistry – A European Journal* 11 (2005) 4983–4994.
- [18] J.C. Groen, G.M. Hamminga, J.A. Moulijn, J. Pérez-Ramírez, *Physical Chemistry Chemical Physics* 9 (2007) 4822–4830.
- [19] J.C. Groen, S. Abelló, L.A. Villaescusa, J. Pérez-Ramírez, *Microporous and Mesoporous Materials* 114 (2008) 93–102.
- [20] J.C. Groen, R. Caicedo-Realpe, S. Abelló, J. Pérez-Ramírez, *Materials Letters* 63 (2009) 1037–1040.
- [21] S. Abelló, A. Bonilla, J. Pérez-Ramírez, *Applied Catalysis A* 364 (2009) 191–198.
- [22] K. Sadowska, A. Wach, Z. Olejniczak, P. Kuśtrowski, J. Datka, *Microporous and Mesoporous Materials* 167 (2013) 82–88.
- [23] B. Gil, Ł. Mokrzycki, B. Sulikowski, Z. Olejniczak, S. Walas, *Catalysis Today* 152 (2012) 24–32.
- [24] J.C. Groen, J.C. Jansen, J.A. Moulijn, J. Pérez-Ramírez, *Journal of Physical Chemistry B* 108 (2004) 13062–13065.
- [25] K. Egeblad, C.H. Christensen, M. Kustova, C.H. Christensen, *Chemistry of Materials* 20 (2008) 946–960.
- [26] J.-B. Koo, N. Jiang, S. Saravanamurugan, M. Bejblova, Z. Musilová, J. Čejka, S.-E. Park, *Journal of Catalysis* 276 (2010) 327–334.
- [27] Y.M. Kustova, S.B. Rasmussen, A.L. Kustov, C.H. Christensen, *Applied Catalysis B* 67 (2006) 60–67.
- [28] A.A. Campus, L. Dimitrov, C.R. da Silva, M. Wallau, E.A. Urquiza-González, *Microporous and Mesoporous Materials* 95 (2006) 92–103.
- [29] M. Choi, K. Na, J. Kim, Y. Sakamoto, O. Terasami, R. Ryo, *Nature* 461/10 (2009) 246–250.
- [30] W. Guo, C. Xiong, L. Huang, Q. Li, *Journal of Materials Chemistry* 11 (2001) 1886–1890.
- [31] Y. Liu, T.J. Pinnavaia, *Journal of Materials Chemistry* 14 (2004) 1099–1103.
- [32] Y. Liu, W. Zhang, T.J. Pinnavaia, *Angewandte Chemie International Edition* 40 (2001) 1255–1258.
- [33] V. Meynen, P. Cool, E.F. Vansant, P. Kortunov, F. Grinberg, J. Kärger, M. Mertens, O.I. Lebedev, G. Van Tendeloo, *Microporous and Mesoporous Materials* 99 (2007) 14–22.
- [34] C.J. Van Oers, W.J.J. Stevens, E. Bruijn, M. Mertens, O.I. Lebedev, G. Van Tendeloo, V. Meynen, P. Cool, *Microporous and Mesoporous Materials* 120 (2009) 29–34.
- [35] V. Meynen, P. Cool, E.F. Vansant, *Microporous and Mesoporous Materials* 125 (2009) 170–223.
- [36] R.B. Borade, A. Clearfield, *Microporous Materials* 5 (1996) 289–297.
- [37] M.L. Kantam, B.P.C. Rao, B.M. Choudary, K.K. Rao, B. Sreedhar, Y. Iwasawa, T. Sasaki, *Journal of Molecular Catalysis A: Chemical* 252 (2006) 76–84.
- [38] L. Li, Q. Shen, J. Li, Z. Hao, Z. Ping Xu, G.Q.M. Lu, *Applied Catalysis A* 344 (2008) 131–141.
- [39] J. Pérez-Ramírez, F. Kapteijn, J.C. Groen, A. Doménech, G. Mul, J.A. Moulijn, *Journal of Catalysis* 214 (2003) 33–45.
- [40] L. Chmielarz, Z. Piwowarska, P. Kuśtrowski, B. Gil, A. Adamski, B. Dudek, M. Michalik, *Applied Catalysis B: Environmental* 91 (2009) 449–459.
- [41] B. Gil, A. Adamski, *Microporous and Mesoporous Materials* 127 (2010) 82–89.
- [42] J. Pérez-Ramírez, M.S. Kumar, A. Brückner, *Journal of Catalysis* 223 (2004) 13–27.
- [43] P. Fejes, I. Kiricsi, K. Lázár, I. Marsi, A. Rockenbauer, L. Korecz, J.B. Nagy, R. Aiello, F. Testa, *Applied Catalysis A – General* 242 (2003) 247–266.
- [44] G.I. Panov, A.K. Uriarte, M.A. Rodkin, V.I. Sobolev, *Catalysis Today* 41 (1998) 365–385.
- [45] K.A. Dubkov, N.S. Ovanesyan, A.A. Shteinman, E.V. Starokon, G.I. Panov, *Journal of Catalysis* 207 (2002) 341–352.
- [46] L. Obalová, V. Fila, *Applied Catalysis B: Environmental* 70 (2007) 353–359.
- [47] G.D. Pirngruber, J.A.Z. Pieterse, *Journal of Catalysis* 273 (2006) 237–247.
- [48] J. Pérez-Ramírez, F. Kapteijn, G. Mul, J.A. Moulijn, *Journal of Catalysis* 208 (2002) 211–223.
- [49] M.N. Debbagh Boutarouch, J.M. García Cortéz, M. Soussi El Bigrani, C. Salinas Martínez de Lecea, J. Pérez-Ramírez, *Applied Catalysis B: Environmental* 54 (2004) 115–123.
- [50] F. Kapteijn, G. Marban, J. Rodríguez-Mirasol, A. Moulijn, *Journal of Catalysis* 167 (1997) 256–265.
- [51] K. Pacultová, L. Obalová, F. Kovanda, K. Jiráková, *Catalysis Today* 137 (2008) 385–389.